BIOCHEMISTRY
including biophysical chemistry & molecular biology

Article

pubs.acs.org/biochemistry

Triphosphate Induced Dimerization of Human Guanylate Binding Protein 1 Involves Association of the C-Terminal Helices: A Joint Double Electron−Electron Resonance and FRET Study

Tobias Vöpel,[†,§,#] Carola S. Hengstenberg,[†,§] Thomas-Otavio Peulen,[∥,§] Yathrib Ajaj,[∥] Claus A. M. Seidel,*[,∥] Christian Herrmann,*[,†] and Johann P. Klare*[,‡]

[†]Physical Chemistry I, Faculty of Chemistry and Biochemistry, Ruhr-University Bochum, Universitätsstrasse 150, 44780 Bochum, Germany

[∥]Chair for Molecular Physical Chemistry, Heinrich-Heine University, Universitätsstrasse 1, 40225 Düsseldorf, Germany

[‡]Macromolecular Structure Group, Department of Physics, University of Osnabrück, Barbarastrasse 7, 49076 Osnabrück, Germany

Supporting Information

ABSTRACT: Human guanylate binding protein 1 (hGBP1) is a member of the dynamin superfamily of large GTPases. During GTP hydrolysis, the protein undergoes structural changes leading to self-assembly. Previous studies have suggested dimerization of the protein by means of its large GTPase (LG) domain and significant conformational changes in helical regions near the LG domain and at its C-terminus. We used site-directed labeling and a combination of pulsed electron paramagnetic resonance and time-resolved fluorescence spectroscopy for structural investigations on hGBP1 dimerization and conformational changes of its C-terminal helix α13. Consistent distance measurements by double electron−electron resonance (DEER, also named pulse double electron resonance = PELDOR) spectroscopy and Förster resonance energy transfer (FRET) measurements using model-free analysis approaches revealed a close interaction of the two α13 helices in the hGBP1 dimer formed upon binding of the nonhydrolyzable nucleoside triphosphate derivate GppNHp. In molecular dynamics (MD) simulations, these two helices form a stable dimer in solution. Our data show that dimer formation of hGBP1 involves multiple spatially distant regions of the protein, namely, the N-terminal LG domain and the C-terminal helices α13. The contacts formed between the two α13 helices and the resulting juxtaposition are expected to be a key step for the physiological membrane localization of hGBP1 through the farnesyl groups attached to the end of α13.

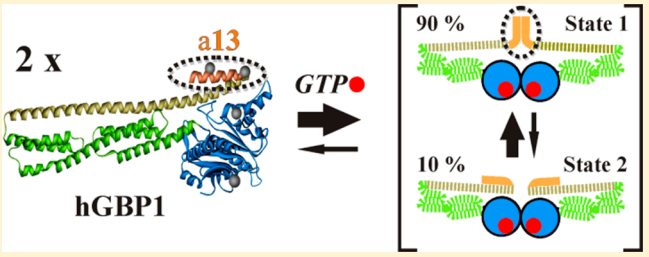

Human guanylate binding protein 1 (hGBP1) belongs to the dynamin superfamily of large GTPases.[1] A common feature of this family of proteins is the nucleotide-dependent assembly to homotypic oligomers, leading to stimulation of the GTPase activity, which in the case of dynamin accounts for scission of vesicles from membranes.[1] In contrast to dynamin, the cellular function of the hGBPs belonging to the same superfamily of large GTPases is only partially understood. Expression of hGBP1 is mainly activated by type II IFN (interferon γ).[2] It participates in immune responses against viral and bacterial targets such as hepatitis C virus, influenza A virus, and bacterial meningitis,[3−8] and exhibits antiangiogenic[9−11] and antitumoral[12−16] activities. The antiangiogenic effects of inflammatory cytokines in cultivated endothelial cells *in vitro*[9,10] and in tumor vessel endothelial cells of colorectal carcinoma patients in vivo[11] have been shown to be mediated by hGBP1. Furthermore, hGBP1 overexpression is associated with different tumor types, such as glioblastoma,[12] oral cancer,[13] and mammary cancer,[14] and was also observed to be associated with paclitaxel drug resistance in ovarian cancer cells and with docetaxel resistance in prostate cancer cells.[15,16]

The elongated 67 kDa protein is generally assumed to consist of three domains (Figure 1A). The LG domain (blue) resembling the canonical GTPase domain of Ras with insertions and extensions is followed by the purely α-helical middle domain (green) and the α12/13 domain (dark yellow/orange) which flanks the full length of the protein. At the C-terminal end the α12/13 domain has contacts with the LG domain, thereby stabilizing its position.[17] hGBP1 can bind all three guanine nucleotides with similar affinities in the low micromolar range.[18−20] It hydrolyzes GTP to GDP and GMP in two successive steps utilizing the same catalytic center.[19,21−24]

Using size exclusion chromatography and dynamic light scattering, it was shown that binding of the nonhydrolyzable GTP analogue GppNHp results in the formation of dimers, and binding of the GTP hydrolysis transition mimic GDP·AlF_x leads to the formation of tetramers.[17] This oligomer formation

Received: April 30, 2014
Revised: July 3, 2014
Published: July 3, 2014

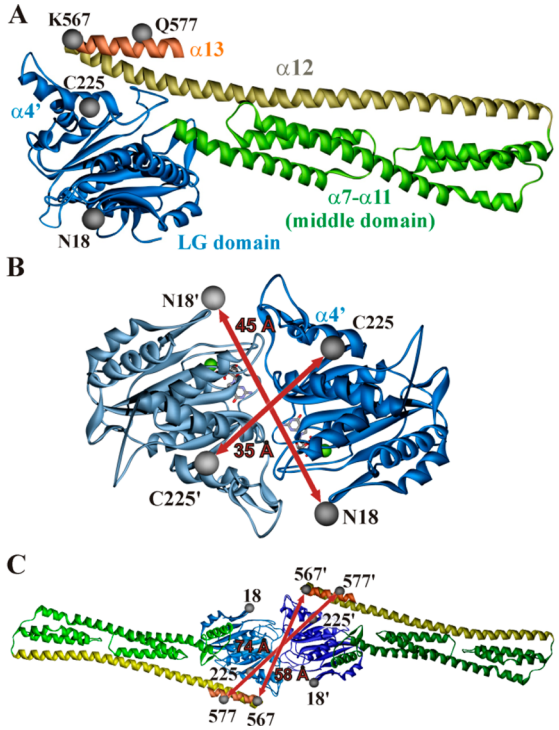

Figure 1. Crystal structures and a model for the dimer of hGBP1. (A) Apo state (pdb: 1DG3).[17] Spin labeled residues are marked by gray spheres at the positions of their Cα atoms. (B) LG domain dimer structure in the presence of GppNHp (pdb: 2BC9).[23] (C) Putative head-to-head dimer model obtained by superimposing the LG domains of the full-length crystal structure in the GppNHp bound state (pdb: 1F5N)[24] onto the LG domains in the dimer structure obtained in the presence of GppNHp (pdb: 2BC9); the expected distances based on this structure are summarized in Table 1.[23] Dark-red arrows and numbers in panels B and C indicate the expected distances (Cα−Cα) based on the crystal structure and the dimer model, respectively.

of hGBP1 triggered by GTP binding leads to a self-stimulation of its GTPase reaction.[25] Therefore, hGBP1 can be categorized as a G protein activated by nucleotide-dependent dimerization.[26] The binding of GppNHp leads to the formation of a putative head-to-head dimer (Figure 1B,C), and structural rearrangements within the LG domain that are believed to be transmitted to α12/13 located at the C-terminus. This in turn is believed to control the oligomerization behavior and the second step of nucleotide hydrolysis.[27−29] However, no detailed structural information on the full length protein in the dimeric or tetrameric state could be obtained so far.

To evaluate the hGBP1 dimer arrangement and possible conformational changes upon dimerization in the GppNHp-bound state, we applied two labeling based techniques for several reasons: (i) to check the consistency between the observations made by electron paramagnetic resonance (EPR) spectroscopy on frozen samples (50 K) and by FRET at physiological temperatures (298 K), (ii) to exclude label-specific effects on the measurements, (iii) to increase the range of accessible distances, and (iv) to take advantage of the method-specific sensitivity ranges for detecting also minor populations that exhibit different structures. Quantitative distance measurements were performed by DEER (PELDOR) spectroscopy[30−34] using site-directed spin labeling (SDSL),[32] and by Förster resonance energy transfer (FRET) using ensemble time-correlated single photon counting (eTCSPC)[35−37] on samples carrying fluorescence labels.

EXPERIMENTAL PROCEDURES

Mutagenesis. All cysteine mutants were constructed based on a cysteine-free hGBP1 variant (C12A/C82A/C225S/C235A/C270A/C311S/C396A/C407S/C589S). All mutants used were generated by QuikChange site directed mutagenesis (Agilent Technologies Sales & Services GmbH &Co.KG, Germany) using templates of hGBP1 in the pQE80L vector (Qiagen GmbH, Germany) as described earlier.[28] All products were verified by DNA sequencing.

Protein Preparation, Spin Labeling, and FRET Labeling. All proteins were expressed from a pQE80L vector (Qiagen GmbH, Germany) in the *Escherichia coli* strain BL21 (DE3). Protein preparations were performed as described.[19] The buffers did not contain any DTE as it would interfere with the following labeling reaction. Concentrations were determined by the protein absorbance at 276 nm (ε_{276} (hGBP1) = 45400 M^{-1} cm^{-1}) according to the method described by Gill and von Hippel.[38]

For the spin labeling reaction, all proteins were incubated with an 8-fold excess of (1-oxyl-2,2,5,5-tetramethylpyrroline-3-methyl) methanethiosulfonate spin label MTSSL (Enzo Life Sciences GmbH, Germany) for 3 h at 4 °C. The reaction was performed in 50 mM Tris, 5 mM $MgCl_2$ solved in D_2O at pH 7.4. Unbound spin labels were removed with Zeba Spin Desalting Columns (Thermo Fisher Scientific GmbH, Germany) equilibrated with 50 mM Tris, 5 mM $MgCl_2$ solved in D_2O at pH 7.4. Concentrations were determined as described above. Labeling efficiencies have been determined by double integration of cw room temperature (RT) EPR spectra in comparison with EPR samples of known concentrations and were ∼90−100% in all cases. In all EPR experiments, the protein concentration was 100 μM.

For labeling with fluorescent dyes proteins were incubated with a 4-fold excess of either Alexa488-C5-maleimide or Alexa647-C2-maleimide (Life Technologies GmbH, Germany) for 1.5 h at 4 °C. The fluorescence labeling buffer had the same composition (solved in H_2O) as described for the spin labeling reaction. Unbound dye was removed with Zeba Spin Desalting Columns (Thermo Fisher Scientific GmbH, Germany). The labeling degree was determined by UV absorption measurements to 70%, 93%, 63%, and 53% for $Q577C^D$, $Q577C^A$, $N18C^D$, and $N18C^A$, respectively.

GTPase Activity. The hydrolytic activity of the different protein mutants was measured by high performance liquid chromatography using a Chromolith Performance RP-18 end-capped column (Merck KGaA, Germany) as described earlier.[27] 2 μM protein was incubated with 350 μM GTP at 25 °C. Samples were analyzed after different reaction periods. The time dependence of the substrate concentration was used to calculate the specific activities of the different protein mutants. The obtained values are given in Supplementary Table S2, Supporting Information.

cw EPR Measurements. Room temperature continuous wave (cw) EPR spectra were recorded on a Miniscope X-band benchtop EPR spectrometer MS200 (Magnetech GmbH, Germany) equipped with a rectangular TE102 resonator. The microwave power was set to 10 mW and the B-field modulation to 0.15 mT. Twenty microliters of sample volume containing 100 μM protein was filled in EPR glass capillaries (0.9 mm inner diameter).

dx.doi.org/10.1021/bi500524u | *Biochemistry* 2014, 53, 4590−4600

Cw EPR spectra for interspin distance determination in the range from ~0.8 to 1.7 nm were obtained on a homemade cw X-band EPR spectrometer equipped with a Super High Sensitivity Probehead (BrukerBiospin GmbH, Germany). The magnetic field was measured with a RMN-2 B-field meter (Drusch GmbH, Germany). A continuous flow cryostat Oxford ESR900 (Oxford Instruments, UK) was used in combination with an Intelligent Temperature Controller ITC 4 (Oxford Instruments, UK) allowing the stabilization of the sample temperature to 160 K. The microwave power was set to 0.2 mW and the B-field modulation amplitude was set to 0.25 mT. EPR quartz capillaries (3 mm inner diameter) were filled with sample volumes of 40 μL. Fitting of simulated dipolar broadened EPR powder spectra to the experimental ones detected at 160 K was carried out using the program ShortDistances by Chr. Altenbach.[39]

Pulse EPR Measurements. Pulse EPR experiments (DEER) were done at X-band frequencies (9.3−9.5 GHz) with a Bruker Elexsys 580 spectrometer equipped with a Bruker Flexline split-ring resonator ER 4118X-MS3 (Bruker Biospin GmbH, Germany) and a continuous flow helium cryostat CF935 (Oxford Instruments, UK) controlled by an Oxford Intelligent Temperature Controller ITC 503S. Sample conditions for the EPR experiments were 100 μM protein in 100 mM NaCl, 50 mM Tris-HCl, 5 mM $MgCl_2$, pH 7.4 dissolved in D_2O with 12.5% (v/v) glycerol-d_8, and 1 mM GDP or 1 mM GppNHp, respectively.

All measurements were performed using the four-pulse DEER sequence: $\pi/2(\upsilon_{obs}) - \tau_1 - \pi\ (\upsilon_{obs}) - t' - \pi\ (\upsilon_{pump}) - (\tau_1 + \tau_2 - t') - \pi\ (\upsilon_{obs}) - \tau_2 -$ echo.[30,31] A two-step phase cycling $(+\langle x\rangle, -\langle x\rangle)$ was performed on $\pi/2\ (\upsilon_{obs})$. Time t' is varied, whereas τ_1 and τ_2 are kept constant, and the dipolar evolution time is given by $t = t' - \tau_1$. Data were analyzed only for $t > 0$. The resonator was overcoupled to $Q \approx 100$; the pump frequency υ_{pump} was set to the center of the resonator dip and coincided with the maximum of the nitroxide EPR spectrum, whereas the observer frequency υ_{obs} was ~65 MHz higher, coinciding with the low field local maximum of the spectrum. All measurements were performed at a temperature of 50 K with observer pulse lengths of 16 ns for $\pi/2$ and 32 ns for π pulses and a pump pulse length of 12 ns. Deuterium modulation was averaged by adding traces at eight different τ_1 values, starting at $\tau_{1,0}$ = 400 ns and incrementing by $\Delta\tau_1$ = 56 ns. Data points were collected in 8 ns time steps or, if the absence of fractions in the distance distribution below an appropriate threshold was checked experimentally, in 16 ns time steps. The total measurement time for each sample was 4−24 h. Analysis of the data was performed with DeerAnalysis 2011[40] using a Tikhonov regularization approach.[41] For details about DEER data analysis, see Supporting Information.

Rotamer Library Analysis. Inter-spin label distance distributions were simulated using a rotamer library of spin labeled residues as described earlier.[42] The rotamer library implemented in the software package MMM2011[41] consisted of 210 rotamers of MTSSL bound to cysteine, which have been used to replace the native residues at the positions of interest in the respective hGBP1 structural models. Energies and resulting populations for individual rotamers were calculated by means of a Lennard−Jones potential at 175 K (the glass transition temperature for a water−glycerol mixture) and have been used as weights in the simulation of the distance distributions. For more details about the RLA, see Supporting Information.

FRET Measurements. Ensemble time-correlated single-photon-counting (eTCSPC) measurements were performed on an IBH-5000U (HORIBA Jobin Yvon IBH Ltd., UK) system. The excitation source was a 470 nm diode laser LDH-P-C 470 (Picoquant GmbH, Germany) operating at 8 MHz for donor excitation. The emission wavelength was set to 520 nm for donor emission. The corresponding monochromator slits were set to 2 nm (excitation path) and 16 nm (emission path) resolution. An additional 500 nm cutoff filter was used to reduce the contribution of the scattered light. All measurements were performed at room temperature under magic-angle with a total protein concentration of approximately 9 μM. The concentration of the donor-labeled protein was 0.5 μM. The actual donor-, acceptor-, and unlabeled-protein concentrations were calculated based on degree of labeling of the individual samples determined by fluorescence and UV-spectroscopy and are summarized in Supplementary Figure S4, Supporting Information. The fluorescence intensity decay curves were fitted using the iterative reconvolution approach.[43] To correct instrumental nonlinearities, the response to uncorrelated light was recorded and considered in the fitting procedure by multiplying the model-function with the normalized/smoothed uncorrelated instrumental response. The fits cover 99.95% of the total fluorescence intensity and start about 500 channels before the laser-pulse recorded in the instrument response function (IRF).

FRET-Accessible Volume Calculations. To describe the behavior of the fluorophore labels on the macromolecules accessible volume (AV), simulations were performed as described previously.[44,37] The accessible volume algorithm implemented in FPSv1.2 calculates all sterically accessible positions given the spatial extension of the dyes (all parameters used are compiled in Supplementary Table S1, Supporting Information). As previously shown, this approach is useful in comparing given model structures with experimental data and can also be used for the generation of new structural models.[45]

Quantitative FRET Analysis: Ensemble TCSPC-Fitting and Determination of the Precision for the Obtained Distances. Under our measurement conditions, we have a mixture of monomeric and dimeric hGBP1. Thus, all donor fluorescence decays $F_D(t)$ were fitted with the decays of at least two molecular species, $F_{D(0)}(t)$ for the donor-/unlabeled protein complexes (DOnly) and $F_{D(A)}(t)$ for the donor-/acceptor-labeled protein complex which is assumed to be dimeric:

$$F(t) = (1 - x_{DOnly})F_{D(A)}(t) + x_{DOnly}F_{D(0)}(t) + c \quad (1)$$

where x_{DOnly} corresponds to the fraction of DOnly molecules and c is a constant offset. Due to local quenching, the fluorescence decay of the donor is triexponential in the absence of FRET with the individual species fractions $x_D^{(i)}$ and fluorescence lifetimes $\tau_{D(0)}^{(i)}$ (see Table S3, Supporting Information):

$$F_{D(0)}(t) = \sum_i x_D^{(i)} \exp(-t/\tau_{D(0)}^{(i)}) \quad (2)$$

Thus, the time-resolved fluorescence intensity decays of donor-/acceptor-labeled protein-complex (FRET sample) were fitted globally with the decays of the donor-/unlabeled protein-complexes (DOnly sample). Generally, it is reasonable to assume that the radiative lifetime of the donor is not affected by quenching. Hence, the FRET-rate constant (k_{FRET}) is

actually only determined by the donor−acceptor distance and their relative orientation.[46] Expressing the FRET rate constant in terms of distances the donor-fluorescence in the presence of acceptor is given by

$$F_{D(A)}(t) = F_{D(0)}\int_{R_{DA}} p(R_{DA})\exp(-tk_0(R_0/R_{DA})^6)\,dR_{DA} \quad (3)$$

Therein $p(R_{DA})$ is a FRET-rate distribution expressed as distance and R_0 is the Förster radius (in this case R_0 = 52 Å) and $k_0 = 1/\tau_0$ is the radiative rate of the unquenched dye.

The fluorophores are attached to the biomolecule by long flexible linkers. Hence, a donor−acceptor distance distribution is expected which is not averaged during the fluorescence lifetime of the dyes,[37] and the fluorescence decay $F_{D(A)}$ has to be expressed as a donor−acceptor distance distribution $p(R_{DA})$ with a nonzero width. Here, the experimental time-resolved fluorescence intensities were either fitted by a Gaussian distribution of donor−acceptor distances ($p(R_{DA})$) with a mean interdye distance $\langle R_{DA}\rangle$ and a width w_{DA} (eq 4) or, analog to the Tikhonov regularization,[40] $p(R_{DA})$ was determined model free by deconvolution of the fluorescence intensity decays by using the maximum-entropy method (MEM).[47,48]

$$F_{D(A)}(t) = F_{D(0)}\int_{R_{DA}} \frac{1}{w_{DA}\sqrt{\pi/2}} \exp\left(-2\left[\frac{R_{DA}-\langle R_{DA}\rangle}{w_{DA}}\right]^2\right)\exp(-tk_0[1+(R_0/R_{DA})^6])\,dR_{DA} \quad (4)$$

The width of the Gaussian donor−acceptor distance distribution w_{DA} should not be misinterpreted as the experimental/statistical-error but it describes a real physical property of the donor−acceptor pair. The experimental fluorescence decays presented below are described by combining the above formulas and were fitted by custom software written in Python.

The fluorescence fractions f_1 and f_2 of the states described by $p_{1,2}(R_{DA})$ are calculated by eq 5.

$$f_{1,2} = \frac{1}{\langle F\rangle}\int p_{1,2}(R_{DA})\frac{1}{k_0}\left(1-\left(1+\left(\frac{R_{DA}}{R_0}\right)^6\right)^{-1}\right)dR_{DA} \quad \text{with } 1 = f_1 + f_2 \quad (5)$$

where $\langle F\rangle$ is used as normalization factor for the total steady state fluorescence intensity.

The parameters and their uncertainties were determined by Markov chain Monte Carlo sampling using the Metropolis−Hasting algorithm.[49,50] All free fitting parameters were sampled using at least 30 individual Markov chains with 150 000 steps each. Each Markov chain started at $\vec{w}_{min}$, whereas $\vec{w}_{min}$ was previously determined by fitting the data with a model function using a conventional Levenberg−Marquardt algorithm. In the case of Gaussian distributed noise on the signal (counts in the TAC-channels) the probability density $P(\vec{m},\vec{w}_i)$ of observing the measurement result $\vec{m}$, given a set of model parameters $\vec{w}_i$, is proportional to $P(\vec{m},\vec{w}_i) \propto \exp(-\chi_i^2(\vec{m},\vec{w}_i)/2)$. Therefore, the probability in the Metropolis algorithm to move from a set of model parameters $\vec{w}_i$ to a new set of model parameters $\vec{w}_{i+1}$ is given by

$$P(\vec{m},\vec{w}_{i\to i+1}) = \exp(-1/2(\chi_{i+1}^2 - \chi_i^2)) \quad (6)$$

with $\vec{w}_{i+1} = \vec{w}_i + \vec{\delta}$. Here $\vec{\delta}$ are Gaussian distributed random values. To reduce the parameter space the Metropolis sampling was restricted to parameters $\vec{w}$ fulfilling $\chi_r^2(\vec{w}) < \chi_{r,max}^2$ with

$$\chi_{r,max}^2(P,\vec{w}_{min}) = \chi_{r,min}^2[1 + n/\nu\cdot cdf^{-1}(F(n,\nu,P))] \quad (7)$$

where cdf^{-1} $(F(n,\nu,P))$ is the inverse of the cumulative distribution function of the F-distribution for n free parameters determined by the dimension of the parameter space, and with ν degrees of freedom given by the number of fitting channels, $\chi_{r,min}^2$ is the minimum determined χ_r^2 (here usually $\chi_{r,min}^2 = \chi_{r,min}^2(\vec{w}_{min})$.[51] If a trial $\vec{w}_{i+1}$ left the region of interest determined by $\chi_{r,max}^2$ the step was neglected and a new trial attempt starting at $\vec{w}_i$ was performed. The presented analysis was at least performed up to the maximum confidence-level of $P_{sample,max} = 1-10^{-5}$. The step-size $\vec{\delta}$ of the Metropolis-Hastings algorithm was adjusted in shorter preruns to obtain an acceptance rate of approximately 60%. After sampling the parameter space samples $\vec{w}_i$ were selected according to their $\chi_r^2(\vec{w}_i)$. Samples with a $\chi_r^2(\vec{w}_i)$ above a maximum chi-square $\chi_{r,max}^2(P_{select,max})$ can be excluded with a confidence level of $P_{select,max}$. The samples with a $\chi_r^2(\vec{w}_i)$ below $\chi_{r,max}^2(P_{select,max})$ define a distribution in the parameter space. The individual fitting parameters are obtained by calculating the mean of their individual marginal distributions, whereas the marginal distributions define the parameter uncertainty.[52]

Construction of the α13 Dimer and Molecular Dynamics (MD) Simulations. The atomic coordinates for helix α13 (residues F565−M583) were extracted from the crystal structure of hGBP1 (pdb: 1F5N).[24] Two such isolated helices were manually oriented in a way that interaction between the hydrophobic faces of the two helices (comprised by residues M572, I576, L579, and M583) was possible (see Figure 4A). The helix dimer was immersed in a water box, at least 12 Å larger than the dimer in any direction, filled with TIP3P water and ∼150 mM sodium and chloride ions, neutralizing the system's net charge. Periodic boundary conditions have been applied. Energy minimization and removal of initial atomic clashes in the starting structure were removed by energy minimization (steepest descent) with the software package Yasara Structure (http://www.yasara.org).[53] After the initial energy minimization, a 100 ns MD simulation was carried out in Yasara, utilizing the Amber03 force field, using Particle Mesh Ewald (PME) summation for long-range electrostatic interactions with a cutoff at 7.86 Å. The time step for the calculation of intramolecular forces was 1.25 fs (simulation substep), intermolecular forces have been calculated every two simulation substeps (2.5 fs). The simulation temperature was 298.0 K. Temperature control was carried out by rescaling atom velocities. Pressure control was achieved by keeping the solvent (H_2O) density at 0.997 g/mL and rescaling the simulation cell along all three axes. Simulation snapshots have been taken each 25 ps.

A second simulation has been carried out using the same starting structure at a temperature of 298.1 K, resulting in different starting velocities for the atoms.

The structure ensemble shown in Figure 4B was prepared by aligning the structures from simulation snapshots taken at 0, 5, 10, ... 100 ns of the 298.0 K trajectory with the MUSTANG algorithm[54] implemented in Yasara Structure.

Analysis of the MD trajectories has been carried out with Yasara. Energies and RMSD values for Cα atoms for the two

dx.doi.org/10.1021/bi500524u | Biochemistry 2014, 53, 4590−4600

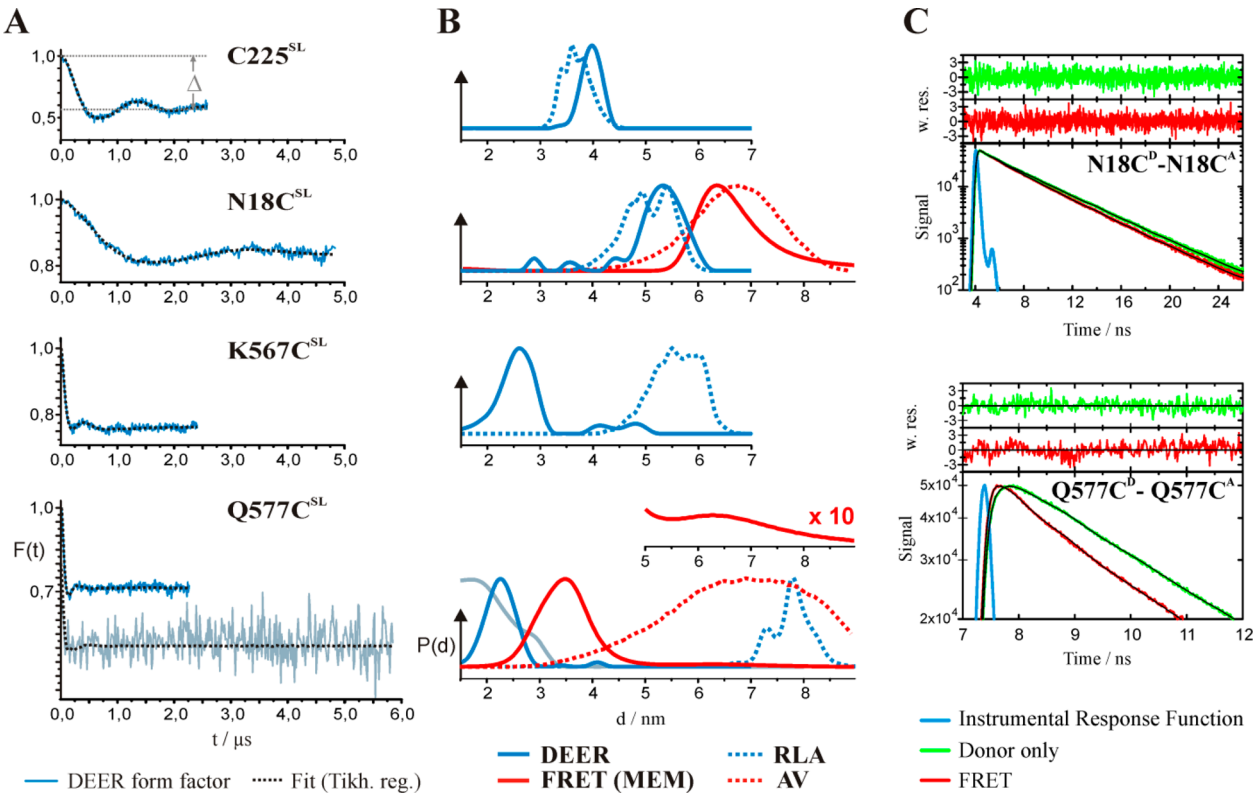

Figure 2. DEER and FRET data. (A) Background corrected DEER traces (form factors, blue) and fits (black) for C225^{SL}, N18C^{SL}, K567C^{SL}, and Q577C^{SL} with GppNHp. In the panel for hGBP1-C225^{SL} the modulation depth Δ is indicated (gray). (B) Distance distributions obtained by Tikhonov regularization (blue) of the DEER data and maximum-entropy deconvolution of the fluorescence decay (red). The inset in the distance distribution for Q577C shows enlarged the second population at 67 Å revealed from the fluorescence data (see text). Dashed lines represent distance distributions obtained by a RLA (blue) and accessible volume (AV) calculations[32] (red) on the model of the full-length dimer in Figure 1C. Abbreviations in graphical legend: MEM, maximum entropy method. (C) Experimental time-resolved donor (D) fluorescence decays (Alexa488) for mixtures with acceptor (A) labeled samples (Alexa647 FRETdecay, red) or unlabeled proteins (U) (DOnly decay, green). The DOnly decays are fitted formally by either two or three lifetimes (eq 3, see Table S3, Suppporting Information), the FRETdecays are fitted by MEM. The weighted residuals of the donor decay and the FRET decay are displayed in the upper panel in green and red, respectively.

simulations are shown in Supplementary Figure S7, Suppporting Information.

RESULTS

Cysteine mutants, based on a cysteine-free hGBP1 variant, were labeled with the MTS spin label (MTSSL) and fluorescence labels, respectively. Four single labeled (SL) hGBP1 constructs were subjected to DEER experiments: hGBP1-N18C^{SL}, -C225^{SL}, -K567C^{SL}, and -Q577C^{SL} (Figure 1A,C). Functionality of the cysteine-free variant Cys-9 and the labeled constructs was verified by their specific GTPase activities, determined as described earlier.[27] All cystein mutants and labeled proteins exhibit either similar or increased (factor 2−3) GTPase activities compared to the hGBP1 wildtype protein (hGBP1 wt, see Supplementary Table S2, Suppporting Information).

First, we confirmed that dimerization of hGBP1 upon binding of GppNHp takes place via the LG domains as suggested from the crystal structure of the isolated LG domains with GppNHp[22] (see Figure 1B). We chose positions 225 on helix α4′, and 18 on the opposite side of the LG domain. The DEER experiments reveal no detectable interspin distances for singly labeled hGBP1 without any nucleotide or with GDP (see Supplementary Figure S1, Suppporting Information). This in accordance with the protein being monomeric, whereas in the presence of GppNHp well-defined inter spin distances are obtained, indicating that the protein forms dimers. Figure 2 shows the results of the DEER experiments for hGBP1-C225^{SL} and hGBP1-N18C^{SL} with bound GppNHp. In Figure 2A the background corrected DEER time traces are shown. Figure 2B depicts the corresponding distance distributions obtained by Tikhonov regularization (for details see Supporting Information and Methods and Figure S1). The distance distribution for position 225 exhibits a single peak at 40 Å. Labels at position 18 on the opposite side of the LG domain show an inter spin distance of 54 Å. Small peaks at shorter distances in the latter case represent noise artifacts and are not reproducible. The observed distances differ by ∼5 Å (pos. 225) and ∼9 Å (pos. 18) from the Cα−Cα distances calculated from the crystal structure (Figure 1B). Nevertheless, when comparing inter spin distances with structural models the length and flexibility of the spin label side chain (Supplementary Figure S2, , Suppporting Information) has to be taken into account. For this purpose, we performed a rotamer library analysis (RLA)[42] on the crystal structure of the isolated LG domain dimer with GppNHp (Figure 1B). In both cases, the calculated distance distributions (Figure 2B; blue, dotted lines) are in good agreement with the experimental data, indicating that the LG domains exhibit an orientation in the hGBP1 dimer resembling the crystal structure of the isolated LG domain dimer (Figure 1B), which has also recently been corroborated by mutational studies.[54] Furthermore, also the widths of the experimental and

dx.doi.org/10.1021/bi500524u | Biochemistry 2014, 53, 4590−4600

RLA calculated distance distributions agree reasonably well. The quality of the data sets (signal-to-noise) and application of the L-curve criterion in the regularization procedure (see Supplementary Experimental Procedures, Supporting Information) give confidence to assume sufficiently high accuracy in prediction of the experimental distance widths for this comparison. This indicates that mainly the mobility of the spin label side chain contributes to the distribution of inter spin distances, as the RLA does not account for protein backbone flexibility. Consequently, the secondary structure elements the labels are attached to are relatively rigid, underlining the stability of the LG domain dimer.

With the given arrangement of the LG domains in the hGBP1 dimer, it is straightforward to construct a model of the full-length dimer by using rigid monomers and superimposing the LG domains of the full-length crystal structure in the GppNHp bound state[24] onto the LG domain dimer structure[23] (Figure 1C). Performing the RLA on this model for positions 567 and 577 reveals calculated distance distributions centered at ∼57 Å and ∼78 Å, respectively (Figure 2B; blue, dotted lines). Surprisingly, the experimental distance distributions (Figure 2B; blue, solid lines) reveal significantly shorter distances, 26 Å for position 567 and 22 Å for position 577. This can only be achieved if α12 and α13 detach from the LG domain and the two α13 helices in the dimer come into close vicinity or associate. Such kind of detachment has already been proposed, first based on the observation that in the presence of GDP·AlF$_x$ (i.e., in the course of GTP hydrolysis) helix α4′ in the LG domain undergoes a conformational change leading to a steric clash with α12/13, and second based on point mutations distorting the contact site between the LG domain and α12/13.[23,27] Our results indicate that the uncoupling between α4′ and α12/13 occurs already upon dimer formation in the presence of GppNHp.

The DEER experiment not only yields a distance distribution but also information about the number of interacting spins,[40] reflected in the modulation depth Δ indicated (gray) for the DEER trace for hGBP1-C225^{SL}. The modulation depth for position 225 corresponds to two interacting nitroxides and consequently >90% dimerization. For hGBP1 spin labeled at positions 18, 567, and 577, respectively, 50%, 64%, and 75% of the proteins show dipolar interaction between the spin labels (the absence of distances <17 Å has been confirmed by cw EPR; see Supplementary Figure S1B, Supporting Information). From protein concentration-dependent GTP hydrolysis activities, an apparent dissociation constant for the hGBP1 dimer is found to be sub-micromolar.[55] Yet, in the case of GppNHp-bound hGBP1 our unpublished data indicate a K_d value around 10 μM. Thus, small differences in the dimer affinities of the four hGBP1 variants together with experimental uncertainties on, e.g., protein concentrations and modulation depths, can explain the variation in the observed dimer populations.

DEER experiments are carried out in frozen solution (50 K), raising the question whether the observed association of the α13 helices takes also place at more physiological temperatures. Quantitative FRET distance measurements by eTCSPC of hGBP1 labeled with fluorescent dyes at positions 18 or 577 at room temperature and comparison of the experimental results to the expectancies given by the structural models corroborated the observation made by DEER.

To study intermolecular FRET, we mixed protein singly labeled with the donor dye Alexa488 (0.5 μM) and the acceptor dye Alexa647 (7.1 μM, 5.1 μM for 577 and 18 respectively). The actual protein concentrations were calculated based on the degree of labeling and the protein concentration determined by UV−vis spectroscopy. The quantitative analysis was performed in two steps: (a) Data analysis using model free and model based approaches combined with accessible volume calculations to determine absolute donor−acceptor distances, (b) determination of the precision and accuracy of the obtained inter dye distances.

To obtain distance distributions in the first step, the fluorescence decay data were analyzed by the model-free method MEM (see Figures 2 and 3), which is equivalent to the Tikhonov regularization in EPR analysis. In the N18C^D-N18C^A sample, an asymmetric peak at position ∼63 Å tailing toward longer distances is observed. The tailing is most likely caused by

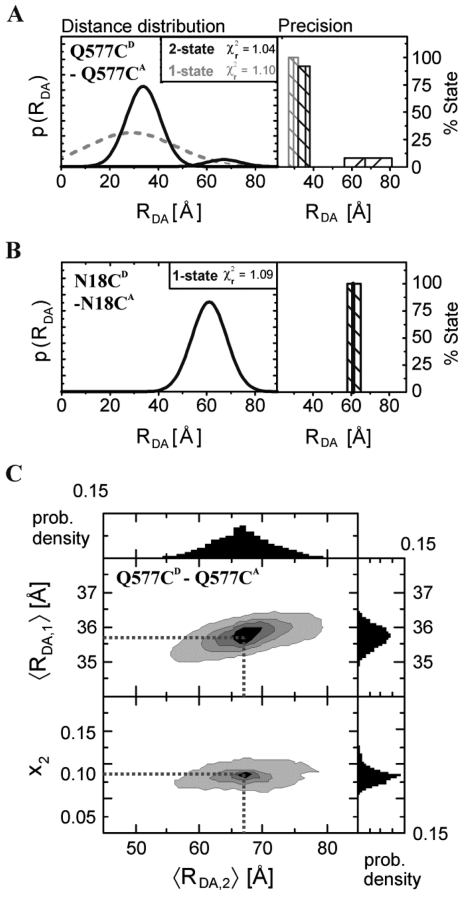

Figure 3. FRET-parameter and error-estimation using Gaussian donor−acceptor distance distributions. (A, B) donor−acceptor distance distributions $p(R_{DA})$ in dependency of the applied fitting model (eq 4). The experimental data was either fitted with a single-state model (gray) or a two-state model (black). By fitting the data with a single-state model a mean-donor−acceptor distance $\langle R_{DA}\rangle$ of 30 ± 3 Å is obtained with a width of w_{DA} = 36.2 ± 6 Å (χ_r^2 = 1.10, confidence-level of 95%). The fit of the data by a two-state model yields the distances $\langle R_{DA,1}\rangle$ = 33 ± 3 Å and $\langle R_{DA,2}\rangle$ = 69 ± 3 Å with a global donor−acceptor distribution width ω_{DA} = 15.4 Å (χ_r^2 = 1.04, confidence-level of 95%). The precision of the fits demonstrates that the results are independent of the applied fitting model and that both distances are well resolved. The fraction of the $\langle R_{DA,2}\rangle$ population is 8 ± 3%. (C) Projections of the probability density of the 2-state model (marginal distributions) of the model parameters $\langle R_{DA,1}\rangle$, $\langle R_{DA,2}\rangle$, and x_2 for a confidence-level 95%. All fit results are summarized in Supplementary Table S3, Supporting Information.

dx.doi.org/10.1021/bi500524u | Biochemistry 2014, 53, 4590−4600

Table 1. Experimental DEER and FRET Mean Distances Compared to Mean Distances Calculated by the Rotamer Library Approach (RLA) for DEER Data and Accessible Volume (AV) Calculations for FRET Data from the Initial Model (2 × 1F5N, Head-to-Head) and from the α13 Dimer (Helix−Helix) Model[a]

		experiment		model			
		distance		1F5N		helix−helix	
technique	sample	mean	w	mean	w	mean	w
EPR[b]	$C225C^{SL}$	40 ± 1	4 ± 2	37	8		
	$N18C^{SL}$	54 ± 1	10 ± 2	50	12		
	$K567C^{SL}$	26 ± 1	8 ± 2	57	12	20	9
	$Q577C^{SL}$	22 ± 1	7 ± 2	78	10	20	12
FRET[c]	$N18C^{D}$-$N18C^{A}$	63 ± 9	14 ± 4	67	16		
	$Q577C^{D}$-$Q577C^{A}$ state 1	35 ± 2	16 ± 4	68	26	32	16
	$Q577C^{D}$-$Q577C^{A}$ state 2	67 ± 12	18 ± 4				

[a]All distances are given in Å. [b]The EPR-model distances are based on the RLA approach. [c]FRET-model distances are based on the AV-approach.

the presence of donor-dyes in absence of acceptor (monomeric proteins). In the $Q577C^{D}$-$Q577C^{A}$ sample, two distinct well separated peaks at ∼35 Å (peak 1) and ∼67 Å (peak 2) are observed. The widths of all peaks determined by MEM are comparable and range from 14 to 18 Å. These widths are within the expectance values for flexible coupled dyes.[37] Compared to model-based approaches MEM has some drawbacks. For instance, the peak width is to some extent determined by the choice of the regularization parameter and depends on the noise level of the data.

To ensure that the second low amplitude peak (∼10%) is justified (signal-to-noise) the L-curve criterion was applied to determine the regularization parameter (see Supplementary Experimental Procedures and Figure S5A−D). Additionally the data were analyzed by model functions where the donor−acceptor distances are Gaussian distributed (see eq 4). The use of simple Gaussians to describe the donor−acceptor distance distributions is justified by the comparison of Gaussian with identical mean and width with distributions calculated by the AV approach and is supported by the maximum entropy method (see Figure 2 and S6 in Suppporting Information). The fit of the $Q577C^{D}$-$Q577C^{A}$ sample using a one-state/distance model results in a mean inter dye distance $\langle R_{DA}\rangle$ = 29 Å and an unusual broad distance distribution with a width of w_{DA} = 36.2 Å (see Figure 3A). This width cannot be explained by dye-linker distributions (see Supplemental Table S1, Suppporting Information). The broadening of the fluorescence signal by dye-linker distributions not averaging out during the fluorescence lifetime of the dye usually only contributes up to a width from 12 to 22 Å.[37] Besides the unusual broad width, a strong correlation of the fitted width and the donor−acceptor distance was observed (see Supplementary Figure S8B, Suppporting Information). Therefore, the experimental data ($Q577C^{D}$-$Q577C^{A}$) was fitted using two Gaussians with a global width w_{DA} and the species fractions x_i. Two populations with mean inter dye distances $\langle R_{DA}\rangle$ of 36 Å (x_1 = 92%) and 67 Å (x_2 = 8%) and a global width of w_{DA} = 15.4 Å were obtained (see Figure 3A). This high sensitivity of fluorescence spectroscopy to minor populations with a high fluorescence quantum yield is given by the fact that the quality of the fit is not weighted by the species fraction of each state x_i but by its fluorescence fraction f_i (see eq 5). For $Q577C^{D}$-$Q577C^{A}$, the fluorescence fraction of the population with the long inter dye distance is significant (f_2 = 0.32) so that it is clearly detectable.

The same analysis was performed also on the data of the $N18C^{D}$-$N18C^{A}$ sample (Figure 3B). In the sample $N18C^{D}$-$N18C^{A}$, no additional broadening beyond the expected dye-linker distribution was observed. Only one Gaussian distributed FRET population ($\langle R_{DA}\rangle$ = 63 ± 9 Å, w_{DA} = 14 ± 4 Å) is needed to describe the decay satisfactorily which agrees well with the MEM analysis in Figure 2.

In the second step of the data analysis, we estimated the precision of the parameter by a Markov chain Monte Carlo sampling as described in the method section. The obtained results are presented in Figure 3C in form of two two-dimensional histograms. These histograms represent possible realizations of the model parameters given a confidence level of $P_{select,max}$ = 95, where the uncertainties correspond to the width of the bar plots in Figure 3A,B.

The accuracy of the inter dye distances is mainly governed by uncertainties of the dye orientation factor κ^2. Independent single-molecule measurements of donor and the acceptor anisotropy (data not shown) show that κ^2 only contributes only by 6% percent to the total uncertainty.[55] Even though the geometric accessible volume approach is a rough approximation of the dye probability distribution, it proved to be a very good estimate in previous studies.[37,44] The results of the accessible volume (AV) simulations[37] (Figure 2B, Supplementary Figure S6, Supporting Information) reveal good agreement for position 18, corroborating the relative LG/LG domain orientation in the dimer, but a strong deviation for the major population in position 577 with the experimental distance being 33 Å shorter compared to the simulation results and well above the estimated errors (Figure 2). To conclude, the precision of the fits demonstrates that the results are independent of the applied fitting model (MEM or Gaussian distance distributions) and both the distances are well resolved.

Consequently, the results of the FRET and DEER measurements which are summarized in Table 1 indicate, within the given experimental errors, the same type of structural alterations. Hence, we conclude that the major mode of dimerization via the LG domains and the conformational change leading to association of the α13 helices prevails also at physiological temperatures.

Being confident that the observed close association of the α13 helices in the hGBP1 dimer is of physiological relevance, we constructed a dimer of two such helices and confirmed by molecular dynamics (MD) simulations that they can form a stable dimer.

Inspection of the primary sequence reveals that one surface of α13 comprises hydrophobic residues (M572, I576, L579, and M583) that could stabilize a parallel helix dimer by van der

dx.doi.org/10.1021/bi500524u | Biochemistry 2014, 53, 4590−4600

Waals interactions. We manually constructed a model with two α13 helices (F565-M583) being in contact via the above-mentioned residues in a parallel orientation (Figure 4A), and performed, after an initial energy minimization, MD simulations in explicit water at 298 K (see Supporting Information).

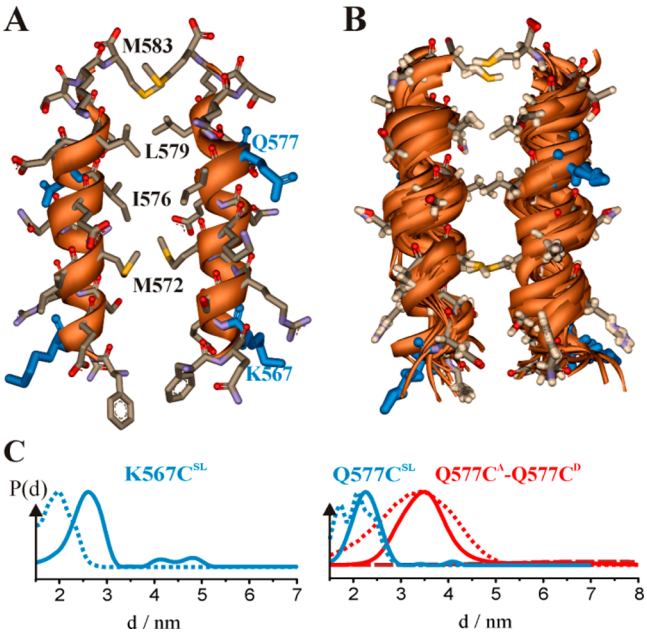

Figure 4. α13 dimer MD simulation. (A) Initial dimer structure after energy minimization. (B) Ensemble of structures from the MD trajectory, taken at simulation times of 0, 5, 10, ..., 100 ns (ribbons) and average structure (ribbon + side chains) calculated from the MD trajectory. (C) Experimental DEER (blue, solid) vs calculated (RLA, blue, dotted) distance distributions from the average dimer structure for K567C^{SL} and Q577C^{SL} (K567 and Q577 are shown in blue in panels a and b) and corresponding FRET data for Q577 (red, solid: experiment (MEM), dotted: calculated (AV)).

The two α13 helices remained reproducibly associated over the whole trajectory length of 100 ns, exhibiting only small fluctuations of the overall dimer arrangement, although the simulations were carried out without any constraints on the atom positions. The persistence of the isolated α13 dimer during the simulations indicates that interaction via this helix could significantly contribute to stabilization of the hGBP1 dimer. Closer inspection of the MD results revealed that interaction between the two helices is mainly conferred by the four hydrophobic side chains mentioned above and depicted in Figure 4A and Supplementary Figure S7, Supporting Information.

Figure 4B shows an ensemble of 21 structures from the MD simulation and an average structure calculated from the MD trajectory. A RLA performed on the latter structure, shown in Figure 4C, yields a calculated distance for K567C^{SL} being ~7 Å shorter compared to the experimentally determined one. A more distant location of the N-terminal ends of the helices than in our α13 dimer model might be caused by their connection to α12, thereby creating additional constraints on the N-termini of the α13 helices that prevent their close interaction. Nevertheless, an almost perfect match of the experimental and the calculated inter spin distances is observed for Q577C^{SL}. Remarkably, here not only the experimental mean distances but also the shape of the distance distribution agrees almost perfectly with the calculations for our α13 dimer model. The calculated distance widths are largely comparable with the experimental distance distributions being broader toward shorter distances. The DEER and FRET results are also consistent for position 577 (Figure 4C, red). Analogous to our interpretation in the case of the LG domain label positions, we suggest the α13 dimer to be rather stable and rigid, corroborating the observed stability of the model in the MD simulations.

DISCUSSION

Dimerization of hGBP1 is triggered by GTP binding and small conformational changes in the LG domain interface. GTP binding alters the conformation of the guanine cap, exposing residues R240 and R244 in a way that a LG domain dimer is formed.[22,54] In another work a buried, hydrophobic helix (α6, P291−S306) in the connecting region between the LG and the middle domain is reported to become exposed upon GTP binding and suggested to mediate dimerization.[56] Using a combination of pulsed EPR and fluorescence spectroscopy based inter label distance measurements with model free analysis approaches for both data sets, we find actually two conformers of the hGBP1 dimer (see Figure 5). For the majorly

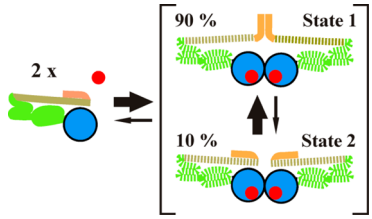

Figure 5. Mechanistic insights—the oligomerization mechanism of the hGBP1 dimer—dashed parts are currently unknown. Blue, LG domain; green, middle-domain; yellow, helix α12; orange, helix α13; red spheres, nucleotide (GTP/GppNHp). The structure of the protein in the apo-form is known and was already solved by X-ray crystallography. Binding of GTP/GppNHp leads to the formation of a putative head-to-head dimer. The protein structure of the nucleotide bond state prior oligomerization is unknown. Experimental data indicate the presence of an equilibrium between dimers with helix α13 contacts (~90%) and the simple putative head-to-head dimers (—10%). Our experimental data do not allow assumptions on the relative orientation of the middle domain and α12; therefore, these protein regions are depicted with higher transparency.

(~90%) populated state 1, we identify a new conformer with another dimerization interface which is formed by the C-terminal helix α13. Moreover, we find a low (~10%) populated state 2 characterized by long distances (67 Å for position 577 from the FRET measurements, ~40−50 Å for K567C^{SL} from DEER) that is well described by the known dimer structure (helix α13 at large distances). We propose that α13 detaches from α12 enabling it to establish additional contacts for dimerization together with α13 from the other hGBP1 molecule. Using a flexible assembly of four rigid domains (LG, middle, α12 and α13) for each molecule, we propose a model for the dimer as illustrated in Figure 5 taking into account all experimental observations of this study. Investigations to clarify the dimerization process as well as conformational changes of the middle domain and helix α12 in the hGBP1 dimer are subject of ongoing research in our groups.

dx.doi.org/10.1021/bi500524u | *Biochemistry* 2014, 53, 4590−4600

Our measurements and simulations suggest that the binding of GppNHp leads to a dimerization of helices α13 (Figure 4). This association brings two lipid modifications into close vicinity as hGBP1 possesses a "CaaX" motif at the end of helix α13 that is farnesylated in vivo.[57,58] In addition, a polybasic sequence directly adjacent to the CaaX box (^{582}KMRRRK^{587}) might further increase membrane affinity.[59,60] Therefore, membrane association, that has already been proposed to be regulated by dimerization,[27,59] might be directly controlled by association of the α13 helices. Recent studies revealed that also hGBP2 and hGBP5 are isoprenylated in vivo and that they can form not only homo- but also heterodimers,[59] suggesting that association of the C-terminal domains might be a general feature of this subclass of GBPs with substantial importance for membrane localization and physiological function.

Finally, we would like to reflect the mechanism of dimer or oligomer formation for members within the dynamin superfamily. It was shown earlier that the LG domain of hGBP1 is essential to form homo dimers and to increase its GTPase activity.[23] Together with our observation of the additional interaction of the α-helical C terminus as illustrated in Figure 4, we find a striking similarity to the dimer structure of bacterial dynamin-like protein (BDLP).[61] It also forms contacts between the G domains, and in addition, between the α-helical, so-called paddle regions at the C-terminus which can be regarded to be homologous to α13 of hGBP1. This close relationship is also reflected in the phylogenetic analysis of the dynamin family members carried out by Low and Löwe on the basis of the LG domain sequences.[61] In contrast, other members of the family of large GTPases form homo-oligomers by a different mechanism. For example, the closely related dynamin and MxA are known to be associated through the helical part of the enzyme in the first place, and LG domain contacts come into play only later.[62−64] Future studies will have to answer the question if and how the two mechanisms of oligomer formation described here are governed by the evolutionary origin of the LG domain.

■ ASSOCIATED CONTENT

Supporting Information

Detailed results of the DEER and FRET data analysis, RLA, AV, and MD simulations. This material is available free of charge via the Internet at http://pubs.acs.org

■ AUTHOR INFORMATION

Corresponding Authors

*(C.A.M.S.) E-mail: cseidel@hhu.de; tel: +49 211 81 15881; fax: +49 211 81 12803.

*(C.H.) E-mail: chr.herrmann@rub.de; tel: +49 234 32 24173; fax: +49 234 32 14785.

*(J.P.K.) E-mail: jklare@uos.de; tel: +49 541 969 2664; fax: +49 541 969 2656.

Present Address

(T.V.) Physical Chemistry II, Faculty of Chemistry and Biochemistry, Ruhr-University Bochum, Universitätsstr. 150, 44780 Bochum, Germany.

Author Contributions

§T.V., C.S.H., and T.O.P. contributed equally.

Funding

Parts of this work were supported by DFG Grant KL2077/1-1 and HE2679/6-1.

Notes

The authors declare no competing financial interest.

■ ACKNOWLEDGMENTS

We thank H.-J. Steinhoff for providing the EPR equipment, fruitful discussions, and reading of the manuscript. Parts of this work were supported by DFG Grant KL2077/1-1 and HE2679/6-1.

■ ABBREVIATIONS

DEER, double electron−electron resonance; EPR, electron paramagnetic resonance; eTCSPC, ensemble time-correlated single-photon counting; FRET, Förster resonance energy transfer; GppNHp, guanosine 5′-imidotriphosphate; hGBP1, human guanylate binding protein 1; MD, molecular dynamics; MTSSL, (1-oxyl-2,2,5,5-tetramethyl-pyrrolinyl-3-methyl) methanethiosulfonate spin label; PELDOR, pulse electron double resonance; RLA, rotamer library analysis; SDSL, site-directed spin labeling

■ REFERENCES

(1) Praefcke, G. J. K., and McMahon, H. T. (2004) The dynamin superfamily: universal membrane tubulation and fission molecules? *Nat. Rev. Mol. Cell. Biol. 5*, 133−147.

(2) Cheng, Y.-S., Colonno, R. J., and Yin, F. H. (1983) Interferon Induction of Fibroblast Proteins with Guanylate Binding Activity. *J. Biol. Chem. 258*, 7746−7750.

(3) Anderson, S. L., Carton, J. M., Lou, J., Xing, L., and Rubin, B. Y. (1999) Interferon-Induced Guanylate Binding Protein-1 (GBP-1) Mediates an Antiviral Effect against Vesicular Stomatitis Virus and Encephalomyocarditis Virus. *Virology 256*, 8−14.

(4) Itsui, Y., Sakamoto, N., Kanikuma, S., Nakagawa, M., Sekine-Osajima, Y., Tasaka-Fujita, M., Nishimura-Sakurai, Y., Suda, G., Karakama, Y., Mishima, K., Yamamoto, M., Watanabe, T., Ueyama, M., Funaoka, Y., Sazuma, S., and Watanabe, M. (2009) Antiviral effects of the interferon-induced protein guanylate binding protein 1 and its interaction with the hepatitis C virus NS5B protein. *Hepatology 50*, 1727−1737.

(5) Naschberger, E., Lubeseder-Martellato, C., Meyer, N., Gessner, R., Kremmer, E., Gessner, A., and Stürzl, M. (2006) Human Guanylate Binding Protein-1 Is a Secreted GTPase Present in Increased Concentrations in the Cerebrospinal Fluid of Patients with Bacterial Meningitis. *Am. J. Pathol. 169*, 1088−1099.

(6) Tietzel, I., El-Haibi, C., and Carabeo, R. A. (2009) Human Guanylate Binding Proteins Potentiate the Anti-Chlamydia Effects of Interferon-γ. *PLoS One 4*, e6499.

(7) Zhu, Z., Shi, Z., Yan, W., Wei, J., Shao, D., Deng, X., Wang, S., Li, B., Tong, G., and Ma, Z. (2013) Nonstructural Protein 1 of Influenza A Virus Interacts with Human Guanylate-Binding Protein 1 to Antagonize Antiviral Activity. *PLoS One 8*, e55920.

(8) Selleck, E., Fentress, Sarah J., Beatty, W. L., Degrandi, D., Pfeffer, K., Virgin, H. W., MacMicking, J. D., and Sibley, L. D. (2013) Guanylate-binding Protein 1 (Gbp1) Contributes to Cell-autonomous Immunity against Toxoplasma gondii. *PLoS Pathogens 9*, e1003320.

(9) Guenzi, E., Töpolt, K., Lubeseder-Martellato, C., Naschberger, E., Benilli, R., Albini, A., and Stürzl, M. (2003) The guanylate binding protein-1 GTPase controls the invasive and angiogenic capability of endothelial cells through inhibition of MMP-1 expression. *EMBO J. 22*, 3772−3782.

(10) Weinländer, K., Naschberger, E., Lehmann, M. H., Tripal, P., Paster, W., Stockinger, H., Hohenadl, C., and Stürzl, M. (2008) Guanylate binding protein-1 inhibits spreading and migration of endothelial cells through induction of integrin α4 expression. *FASEB J. 22*, 4168−4178.

(11) Naschberger, E., Croner, R. S., Merkel, S., Dimmler, A., Tripal, P., Amann, K. U., Kremmer, E., Brueckl, W. M., Papadopoulos, T., Hohenadl, C., Hohenberger, W., and Stürzl, M. (2008) Angiostatic

immune reaction in colorectal carcinoma: Impact on survival and perspectives for antiangiogenic therapy. *Int. J. Cancer 123*, 2120−2129.
(12) Li, M., Mukasa, A., del-Mar Inda, M., Zhang, J., Chin, L., Cavenee, W., and Furnari, F. (2011) Guanylate binding protein 1 is a novel effector of EGFR-driven invasion in glioblastoma. *J. Exp. Med. 208*, 2657−2673.
(13) Yu, C. J., Chang, K. P., Chang, Y. J., Hsu, C. W., Liang, Y., Yu, J. S., Chi, L. M., Chang, Y. S., and Wu, C. C. (2011) Identification of Guanylate-Binding Protein 1 as a Potential Oral Cancer Marker Involved in Cell Invasion Using Omics-Based Analysis. *J. Proteome Res. 10*, 3778−3788.
(14) Lipnik, K., Naschberger, E., Gonin-Laurent, N., Kodajova, P., Petznek, H., Rungaldier, S., Asigiano, S., Ferrini, S., Stürzl, M., and Hohenadl, C. (2010) Interferon γ−Induced Human Guanylate Binding Protein 1 Inhibits Mammary Tumor Growth in Mice. *Mol. Med. 16*, 177−187.
(15) Desarnaud, F., Geck, P., Parkin, C., Carpinito, G., and Makarovskiy, A. N. (2011) Gene expression profiling of the androgen independent prostate cancer cells demonstrates complex mechanisms mediating resistance to docetaxel. *Cancer Biol. Ther. 11*, 204−212.
(16) Duan, Z., Foster, R., Brakora, K. A., Yusuf, R. Z., and Seiden, M. V. (2006) GBP1 overexpression is associated with a paclitaxel resistance phenotype. *Cancer Chemother. Pharmacol. 57*, 25−33.
(17) Prakash, B., Praefcke, G. J. K., Renault, L., Wittinghofer, A., and Herrmann, C. (2000) Structure of human guanylate-binding protein 1 representing a unique class of GTP-binding proteins. *Nature 403*, 567−571.
(18) Cheng, Y.-S., Becker-Manley, M. F., Chow, T. P., and Horan, D. C. J. (1985) Affinity purification of an interferon-induced human guanylate-binding protein and its characterization. *Biol. Chem. 260*, 15834−15839.
(19) Praefcke, G. J. K., Geyer, M., Schwemmle, M., Kalbitzer, H. R., and Herrmann, C. (1999) Nucleotide-binding characteristics of human guanylate-binding protein 1 (hGBP1) and identification of the third GTP-binding motif. *J. Mol. Biol. 292*, 321−332.
(20) Praefcke, G. J. K., Kloep, S., Benscheid, U., Lilie, H., Prakash, B., and Herrmann, C. (2004) Identification of Residues in the Human Guanylate-binding Protein 1 Critical for Nucleotide Binding and Cooperative GTP Hydrolysis. *J. Mol. Biol. 344*, 257−269.
(21) Cheng, Y.-S., Patterson, C. E., and Staeheli, P. (1991) Interferon-induced guanylate-binding proteins lack an N(T)KXD consensus motif and bind GMP in addition to GDP and GTP. *Mol. Cell. Biol. 11*, 4717−4725.
(22) Kunzelmann, S., Praefcke, G. J. K., and Herrmann, C. (2006) Transient Kinetic Investigation of GTP Hydrolysis Catalyzed by Interferon-g-induced hGBP1 (Human Guanylate Binding Protein 1). *J. Biol. Chem. 281*, 28627−28635.
(23) Ghosh, A., Praefcke, G. J. K., Renault, L., Wittinghofer, A., and Herrmann, C. (2006) How guanylate-binding proteins achieve assembly-stimulated processive cleavage of GTP to GMP. *Nature 440*, 101−104.
(24) Prakash, B., Renault, L., Praefcke, G. J. K., Herrmann, C., and Wittinghofer, A. (2000) Triphosphate structure of guanylate-binding protein 1 and implications for nucleotide binding and GTPase mechanism. *EMBO J. 19*, 4555−4564.
(25) Kunzelmann, S., Praefcke, G. J. K., and Herrmann, C. (2005) Nucleotide Binding and Self-Stimulated GTPase Activity of Human Guanylate-Binding Protein 1 (hGBP1). *Methods Enzymol. 404*, 512−527.
(26) Gasper, R., Meyer, S., Gotthardt, K., Sirajuddin, M., and Wittinghofer, A. (2009) It takes two to tango: regulation of G proteins by dimerization. *Nat. Rev. Mol. Cell. Biol. 10*, 423−429.
(27) Vöpel, T., Syguda, A., Britzen-Laurent, N., Kunzelmann, S., Lüdemann, M. B., Dovengerds, C., Stürzl, M., and Herrmann, C. (2010) Mechanism of GTPase activity induced self-assembly of human guanylate binding protein 1. *J. Mol. Biol. 400*, 63−70.
(28) Vöpel, T., Kunzelmann, S., and Herrmann, C. (2009) Nucleotide dependent cysteine reactivity of hGBP1 uncovers a domain movement during GTP hydrolysis. *FEBS Lett. 583*, 1923−1927.
(29) Syguda, A., Bauer, M., Benscheid, U., Ostler, N., Naschberger, E., Ince, S., Stürzl, M., and Herrmann, C. (2012) Tetramerisation of human guanylate binding protein 1 is mediated by coiled coil formation of the C-terminal α-helices. *FEBS J. 279*, 2544−2554.
(30) Martin, R. E., Pannier, M., Diederich, F., Gramlich, V., Hubrich, M., and Spiess, H. W. (1998) Determination of End-to-End Distances in a Series of TEMPO Diradicals of up to 2.8 nm Length with a New Four-Pulse Double Electron Electron Resonance Experiment. *Angew. Chem. Int. Ed. 37*, 2833−2837.
(31) Pannier, M., Veit, S., Godt, A., Jeschke, G., and Spiess, H. W. (2000) Dead-Time Free Measurement of Dipole-Dipole Interactions between Electron Spins. *J. Magn. Reson. 142*, 331−340.
(32) Klare, J. P., and Steinhoff, H.-J. (2009) Spin Labeling EPR. *Photosynth. Res. 102*, 377−390.
(33) Meyer, S., Böhme, S., Krüger, A., Steinhoff, H.-J., Klare, J. P., and Wittinghofer, A. (2009) Kissing G domains of MnmE monitored by X-ray crystallography and pulse EPR Spectroscopy. *PLoS Biol. 7*, e1000212.
(34) Böhme, S., Meyer, S., Krüger, A., Steinhoff, H.-J., Wittinghofer, A., and Klare, J. P. (2010) Stabilization of G domain conformations in the tRNA modifying MnmE/GidA complex observed with DEER spectroscopy. *J. Biol. Chem. 285*, 16991−17000.
(35) Kravets, E., Degrandi, D., Weidtkamp-Peters, S., Konermann, C., Felekyan, S., Darkazanli, J. M., Praefcke, G. J., Seidel, C. A., Schmitt, L., Smits, S. H., and Pfeffer, K. J. (2012) The GTPase activity of murine guanylate-binding protein 2 (mGBP2) controls the intracellular localization and recruitment to the parasitophorous vacuole of *Toxoplasma gondii*. *J. Biol. Chem. 287*, 27452−27466.
(36) Rothwell, P. J., Berger, S., Kensch, O., Felekyan, S., Antonik, M., Wöhrl, B. M., Restle, T., Goody, R. S., and Seidel, C. A. M. (2003) Multiparameter single-molecule fluorescence spectroscopy reveals heterogeneity of HIV-1 reverse transcriptase:primer/template complexes. *Proc. Natl. Acad. Sci. U.S.A. 100*, 1655−1660.
(37) Sindbert, S., Kalinin, S., Nguyen, H., Kienzler, A., Bannwarth, W., Appel, B., Müller, S., and Seidel, C. A. M. (2011) Accurate Distance Determination of Nucleic Acids via Förster Resonance Energy Transfer: Implications of Dye Linker Length and Rigidity. *J. Am. Chem. Soc. 133*, 2463−2480.
(38) Gill, S. C., and von Hippel, P. H. (1989) Calculation of protein extinction coefficients from amino acid sequence data. *Anal. Biochem. 182*, 319−326.
(39) Altenbach, C., https://sites.google.com/site/altenbach/labview-programs/epr-programs/short-distances.
(40) Jeschke, G., Chechik, V., Ionita, P., Godt, A., Zimmermann, H., Banham, J. E., Timmel, C. R., Hilger, D., and Jung, H. (2006) DeerAnalysis2006 - a comprehensive software package for analyzing pulsed ELDOR data. *Appl. Magn. Reson. 30*, 473−498.
(41) Tikhonov, A. N., and Arsenin, V. Y. (1977) *Solutions of Ill-Posed Problems*, Wiley, New York.
(42) Polyhach, Y., Bordignon, E., and Jeschke, G. (2011) Rotamer libraries of spin labelled cysteines for protein studies. *Phys. Chem. Chem. Phys. 13*, 2356−2366.
(43) O'Connor, D. V., and Phillips, D. (1984) *Time-Correlated Single Photon Counting*, Academic Press, New York.
(44) Muschielok, A., Andrecka, J., Jawhari, A., Bruckner, F., Cramer, P., and Michaelis, J. (2008) A nano-positioning system for macromolecular structural analysis. *Nature Methods 5*, 965−971.
(45) Kalinin, S., Peulen, T., Sindbert, S., Rothwell, P. J., Berger, S., Restle, T., Goody, R. S., Gohlke, H., and Seidel, C. A. M. (2012) A toolkit and benchmark study for FRET-restrained high-precision structural modeling. *Nat. Methods 9*, 1218−1225.
(46) Kalinin, S., and Johansson, L. B. (2004) Energy Migration and Transfer Rates Are Invariant to Modeling the Fluorescence Relaxation by Discrete and Continuous Distributions of Lifetimes. *J. Phys. Chem. B 108*, 3092−3097.
(47) Livesey, A. K., and Skilling, J. (1985) Maximum Entropy Theory. *Acta Crystallogr., Sect. A 41*, 113−122.

(48) Brochon, J. C. (1994) Maximum entropy method of data analysis in time-resolved spectroscopy. *Methods Enzymol. 240*, 262−311.
(49) Metropolis, N., Rosenbluth, A., Rosenbluth, M., Teller, A., and Teller, E. (1953) Equation of State Calculations by Fast Computing Machines. *J. Chem. Phys. 21*, 1087−1092 S..
(50) Hastings, W. K. (1970) Monte Carlo sampling methods using Markov chains and their applications. *Biometrika 57*, 97−109 S..
(51) Lakowicz, J. R. (2006) *Principles of Fluorescence Spectroscopy*, 3rd ed., Springer, New York.
(52) Gregory, P. (2005) *Baysian Logical Data Analysis for the Physical Sciences*, Cambridge University Press, New York.
(53) Krieger, E., Koraimann, G., and Vriend, G. (2002) Increasing the precision of comparative models with YASARA NOVA - a self-parameterizing force field. *Proteins 47*, 393−402.
(54) Konagurthu, A. S., Whisstock, J. C., Stuckey, P. J., and Lesk, A. M. (2006) MUSTANG: A multiple structural alignment algorithm. *Proteins 64*, 559−574.
(55) Wehner, M., Kunzelmann, S., and Herrmann, C. (2012) The guanine cap of hGBP1 is responsible for dimerization and self-activation of GTP hydrolysis. *FEBS J. 279*, 203−210.
(56) Dale, R. E., Eisinger, J., and Blumberg, W. E. (1979) Theorientational freedom of molecular probes orientation factor in intramolecular energy transfer. *Biophys. J. 26*, 161−193.
(57) Abdullah, N., Balakumari, M., and Sau, A. K. (2010) Dimerization and Its Role in GMP Formation by Human Guanylate Binding Proteins. *Biophys. J. 99*, 2235−2244.
(58) Nantais, D. E., Schwemmle, M., Stickney, J. T., Vestal, D. J., and Buss, J. E. (1996) Prenylation of an interferon-gamma-induced GTP-binding protein: the human guanylate binding protein, huGBP1. *J. Leukoc. Biol. 60*, 423−431.
(59) Britzen-Laurent, N., Bauer, M., Berton, V., Fischer, N., Syguda, A., Reipschläger, S., Naschberger, E., Herrmann, C., and Stürzl, M. (2010) Intracellular Trafficking of Guanylate-Binding Proteins Is Regulated by Heterodimerization in a Hierarchical Manner. *PLoS One 5*, e14246.
(60) Hancock, J. F., Paterson, H., and Marshall, C. J. (1990) A polybasic domain or palmitoylation is required in addition to the CAAX motif to localize p21ras to the plasma membrane. *Cell 63*, 133−139.
(61) Wright, L. P., and Philips, M. R. (2006) CAAX modification and membrane targeting of Ras. *J. Lipid Res. 47*, 883−891.
(62) Low, H. H., and Löwe, J. (2006) A bacterial dynamin-like protein. *Nature 444*, 766−769.
(63) Ford, M. G. J., Jenni, S., and Nunnari, J. (2011) The crystal structure of dynamin. *Nature 477*, 561−566.
(64) Chappie, J. S., Mears, J. A., Fang, S., Leonard, M., Schmid, S. L., Milligan, R. A., Hinshaw, J. E., and Dyda, F. (2011) A pseudoatomic model of the dynamin polymer identifies a hydrolysis-dependent powerstroke. *Cell 147*, 209−222.
(65) Gao, S., von der Malsburg, A., Dick, A., Faelber, K., Schröder, G. F., Haller, O., Kochs, G., and Daumke, O. (2011) Structure of myxovirus resistance protein A reveals intra- and intermolecular domain interactions required for the antiviral function. *Immunity 35*, 514−525.